catalysts

MDPI

Article

Block Copolymer and Cellulose Templated Mesoporous TiO_2-SiO_2 Nanocomposite as Superior Photocatalyst

Sudipto Pal [1,*], Antonietta Taurino [2], Massimo Catalano [2] and Antonio Licciulli [1,3]

[1] Department of Engineering for Innovation, University of Salento, Via per Monteroni, 73100 Lecce, Italy; antonio.licciulli@unisalento.it
[2] Institute for Microelectronics and Microsystems (IMM), CNR, Via Monteroni, 73100 Lecce, Italy; antonietta.taurino@le.imm.cnr.it (A.T.); massimo.catalano@le.imm.cnr.it (M.C.)
[3] Institute of Nanotechnology, CNR Nanotec, Consiglio Nazionale Delle Ricerche, Via Monteroni, 73100 Lecce, Italy
* Correspondence: sudipto.pal@unisalento.it

Abstract: A dual soft-templating method was developed to produce highly crystalline and mesoporous TiO_2-SiO_2 nanocomposites. Pluronic F127 as the structure-directing agent and pure cellulose as the surface area modifier were used as the templating media. While Pluronic F127 served as the sacrificing media for generating a mesoporous structure in an acidic pH, cellulose templating helped to increase the specific surface area without affecting the mesoporosity of the TiO_2-SiO_2 nanostructures. Calcination at elevated temperature removed all the organics and formed pure inorganic TiO_2-SiO_2 composites as revealed by TGA and FTIR analyses. An optimum amount of SiO_2 insertion in the TiO_2 matrix increased the thermal stability of the crystalline anatase phase. BET surface area measurement along with low angle XRD revealed the formation of a mesoporous structure in the composites. The photocatalytic activity was evaluated by the degradation of Rhodamine B, Methylene Blue, and 4-Nitrophenol as the model pollutants under solar light irradiation, where the superior photo-degradation activity of Pluronic F127/cellulose templated TiO_2-SiO_2 was observed compared to pure Pluronic templated composite and commercial Evonik P25 TiO_2. The higher photocatalytic activity was achieved due to the higher thermal stability of the nanocrystalline anatase phase, the mesoporosity, and the higher specific surface area.

Keywords: TiO_2-SiO_2; mesoporous; F127; high surface area; solar photocatalysis; dye degradation

Citation: Pal, S.; Taurino, A.; Catalano, M.; Licciulli, A. Block Copolymer and Cellulose Templated Mesoporous TiO_2-SiO_2 Nanocomposite as Superior Photocatalyst. *Catalysts* **2022**, *12*, 770. https://doi.org/10.3390/catal12070770

Academic Editors: Magdalena Zybert and Katarzyna Antoniak-Jurak

Received: 16 May 2022
Accepted: 8 July 2022
Published: 12 July 2022

1. Introduction

Water contamination from the wastewater released by the textile industries, pharmaceutical plants, and agrochemical and leather processing factories is one of the biggest concerns among the various forms of environmental pollution [1,2]. A large number of organic dyes are currently used for various purposes, e.g., Rhodamine B and Methylene Blue as colorants and 4-Nitrophenol for manufacturing drugs and pesticides. Most of them are highly water soluble and non-biodegradable, and therefore difficult to separate by filtering processes. Among the various degradation techniques, photocatalytic mineralization is one of the best environmental-friendly techniques, since other chemical/biological processes can produce secondary byproducts [3]. Titanium dioxide (TiO_2) with a stable anatase crystalline phase is considered to be one of the best photocatalyst materials, which is widely used in the photodecomposition of organic pollutants, wastewater treatment, and environmental remediations [1,4–7]. A higher photocatalytic activity, long term photo and chemical stability, low toxicity, and relatively lower cost make it an excellent candidate in heterogeneous photocatalysis [8,9]. The basic principle of photocatalysis in TiO_2 relies on the formation of excitons (electron-hole pairs) generated by the excitation of the absorbed photon energy that is greater than the band gap energy of TiO_2 (3.0–3.2 eV) and their migration to the catalyst surface. These photogenerated excitons may take place in the

redox reactions where superoxide radical anions ($O_2^{\bullet -}$) and hydroxyl radicals ($OH^{\bullet}$) are produced in the presence of oxygen and water, and later on in the process end up with the mineralization of the organic species adsorbed on TiO_2 surfaces [10–12]. The photocatalytic efficiency of TiO_2 depends on several factors such as crystalline phase, particle size, specific surface area, and porosity [13]. The high crystallinity in TiO_2 enhances the generation and migration of the photogenerated excitons, whereas its higher surface area and mesoporosity help to enhance its reactivity by means of increasing the active sites [10,14]. Moreover, the higher surface area along with mesoscale porosity could trap the contaminants/molecules into their porous and well-connected network, which could initiate the photocatalytic reaction process very quickly.

The soft-templating route wherein non-ionic (such as triblock copolymers, Pluronic F127, P123) [15] or ionic (such as CTAB) [16] surfactants are used as the scarifying media for regular pore generation is the most popular way to synthesize mesoporous metal oxide nanomaterials. After burning out these surfactants at a certain temperature, the mesoporous structure is retained by the synthesized oxide nanomaterial. The mesoporous nanocrystalline TiO_2, either in powder form or thin film, synthesized following this route has been reported [17–19]. However, due to the prolonged calcination process at elevated temperatures, which are necessary to obtain the mesoporous structure, TiO_2 often suffers from the anatase to rutile phase transformation (due to thermal instability of the anatase phase) that hinders its photocatalytic activity [18,20–22]. This could be avoided by incorporating silica (SiO_2) into the titania matrices [14,23–25]. Silica insertion into the TiO_2 nanostructure not only increases the thermal stability of the highly photoactive anatase phase but also helps to prevent the mesoporous structure from collapsing [2,26–28]. Introducing cellulose matrix as the second templating media to the triblock copolymer-TiO_2-SiO_2 composite could further enhance the specific surface area and support the mesoporous structure with a higher degree of dispersibility in aqueous media that would enhance the photocatalytic efficiency [29]. Due to the 3D web-like nanofibrous structure of cellulose, there has been significant interest in synthesizing cellulose-TiO_2 nanocomposites, either by the immobilization of TiO_2 on cellulose or by using as template [29–33]. However, most of the preparation methods need either multistep stages or take a prolonged period to obtain the composite mesoporous nanostructure. In this work, we have demonstrated a quick procedure to anchor the TiO_2-SiO_2-triblock copolymer composite on a cellulose (commercial filter paper) matrix and obtain pure inorganic TiO_2-SiO_2 mesoporous nanostructure after burning out the cellulose template and the copolymer as well. In this unique templating method, the triblock copolymer acts as the structure-directing and mesopore-generating agent, whereas the SiO_2 counterpart fixes the thermal stability of the anatase phase and the mesostructure, and finally the cellulose templating enhances the specific surface area and porosity. The obtained TiO_2-SiO_2 nanocomposites showed excellent thermal stability of the anatase phase and a higher photocatalytic efficiency as compared to the commercial P25 TiO_2.

2. Materials and Methods

2.1. Preparation of the Photocatalyst

All the reagents involved in the catalyst synthesis were used as received without making any further modifications. Triblock copolymer Pluronic F127 (EO_{106} PO_{70} EO_{106}, average molecular weight 12.6 kDa, Sigma-Aldrich, Saint Louis, MO, USA), titanium tetraisopropoxide ($Ti(O^iPr)_4$, TTIP, 97%), tetraethoxysilane ($Si(OC_2H_5)_4$, TEOS, 97%, Sigma-Aldrich, Saint Louis, MO, USA), hydrochloric acid (HCl, 37–38%, J.T. Baker), and Whatman filter paper (qualitative, grade 595) were used as the reagents. Commercial P25 TiO_2 nanopowder was purchased from Evonik Resource Efficiency GmbH (Hanau-Wolfgang, Hesse, Germany). First, TiO_2-SiO_2 composites with different TiO_2/SiO_2 weight ratios were synthesized according to our previous work with a little modification [34]. As in a typical synthesis of TS82, the required amount of F127 (0.012 M of oxides) was dissolved in 600 g of 2 M HCl and 150 g of water with vigorous stirring. After obtaining a clear solution, TEOS was added drop wise followed by stirring for 1 h and then TTIP was slowly added

to the mixture followed by overnight stirring for a hydrolysis-condensation reaction. Then, the mixed sol was transferred to a polypropylene bottle and kept in an oven at 80 °C for 48 h. Then, the solid precipitate was separated and dried to form the xerogel, followed by calcination at 550 °C for 6 h with a heating and cooling rate of 1 °C/min to remove the organic contents. It is to be noted that the highest photocatalytic efficiency was achieved with the TS82 sample [35] (Figure S3, Table S2), so only this composition was chosen to prepare the cellulose-TiO_2/SiO_2 nanocomposite, which is denoted as TS82C throughout this article. To obtain this, the filter papers were cut into pieces and impregnated during the hydrolysis–condensation process and followed the procedure as described above with the similar heating cycle. After removal of all organics, thin flakes of TS82C with bright white colour were obtained.

2.2. Characterizations

Crystalline phases of the nanocomposite powder samples were characterized by wide angle (10–80° 2θ) X-ray diffraction (XRD) spectrometry performed on a Rigaku Ultima X-ray diffractometer using Cu*K*α radiation (λ = 1.5406 Å) operating at 40 kV/30 mA with a step size of 0.02°. The low angle (0.3–10° 2θ) XRD pattern (GIXRD) was collected with a Rigaku SmartLab diffractometer operating at 9 kW. Thermogravimetric analysis (TGA) was carried out with a Mettler thermo-analyzer (Mettler Toledo, Star system) at a heating rate of 5 °C/min in an air atmosphere. FTIR spectra of the obtained composite was carried out with a JASCO FTIR-6300 over the range of 4000–400 cm^{-1} with a resolution of 4 cm^{-1} and accumulating 256 scans for each measurement adopting the KBr disc method. Raman spectral measurements (FT-Raman) of the powders were performed on a JASCO RFT-6000 Raman attachment by using a 1064 nm CW 500 mW laser source and spectral resolution of 4 cm^{-1}. Surface area and porosity of the samples were measured from nitrogen adsorption–desorption isotherms at liquid nitrogen temperature (77 K) by using a Quantachrome NOVA 2200e surface area and pore size analyzer. Before each measurement, the powder samples were degassed overnight at 423 K under nitrogen flow. The specific surface area was calculated by the multipoint BET (Brunauer–Emmett–Teller) equation from the N_2 adsorption branch of the isotherm in the relative pressure range of 0.05–0.35. The pore size distribution was calculated using the Barret–Joyner–Halenda (BJH) method from the desorption branch of the isotherm. FESEM measurements were performed with a Zeiss Sigma VP (Carl Zeiss, Jena, Germany) field emission scanning electron microscope. Transmission electron microscopic (TEM) analyses were performed with a JEOL JEM-1011 transmission electron microscope operating at 100 kV and equipped with a 7.1-megapixel CCD camera (Orius SC1000, Gatan, Pleasanton, CA, USA). The TEM micrographs were processed with Gatan's Digital Micrograph (DM) software. Average particle size was determined by counting 50 particles from two different micrographs.

2.3. Photocatalytic Experimental Set Up

Photocatalytic efficiency of the synthesized nanocomposites was tested by observing the degradation of rhodamine B (RhB), methylene blue (MB), and 4-Nitrophenol (4NP) aqueous solution under solar light irradiation (A single 300 W tungsten lamp with spectral irradiance of 13.6 W/m^2 and 41.4 W/m^2 in the wavelength range of 315–400 nm and 380–780 nm, respectively). The distance from the bottom of the lamp to the upper level of the dye solution was maintained at about 30 cm. In each case, prior to the solar light exposure, the composite powder samples (1 g/L) were dispersed in respective aqueous solutions of the dye molecules (200 mL, 15×10^{-6} M) and stirring was continued for 18 h in dark conditions to ensure the adsorption–desorption equilibrium. Then, they were kept under solar light irradiation and stirred constantly, and aliquot amounts (1 mL) of the irradiated solutions were extracted at 5 min intervals. Photocatalytic decomposition was monitored by measuring the absorption band of the respective dye solutions with an Agilent Cary 5000 series UV-Visible spectrophotometer. In all cases, prior to the optical measurement, the catalysts were separated from the solution by high-speed centrifugation.

3. Results and Discussion

3.1. Thermogravimetric Analyses and FTIR

The thermal decomposition behavior of the cellulose-titania/silica composite was investigated by thermogravimetric analysis (TGA), which is presented in Figure 1a. The TGA curve shows a gradual weight loss with an increasing calcination temperature. A small weight loss (3.45%) below 110 °C is seen at the first step, which is due to the loss of some volatile species such as water, ethanol/propanol, and HCl [19,36]. Then, an 18.8% weight loss was observed in the temperature range of 200–254 °C, which stems from the decomposition of the F127 template [20,37]. The steep decrease (weight loss 49.61%) up to 340 °C could be due to the carbonization of the cellulose template [30,32,38]. The weight loss (13.64%) at the final step from 340–420 °C could be attributed to the decomposition of some residual hydroxyl group or oxidation of the carbonaceous species and possibly the transformation of amorphous titania to anatase phase [19,38]. After that, no changes in weight loss were observed, indicating the complete removal of both the templates and high temperature stability of the nanocomposite. As we have performed thermal treatment at 550 °C, no organic residue was present in our sample.

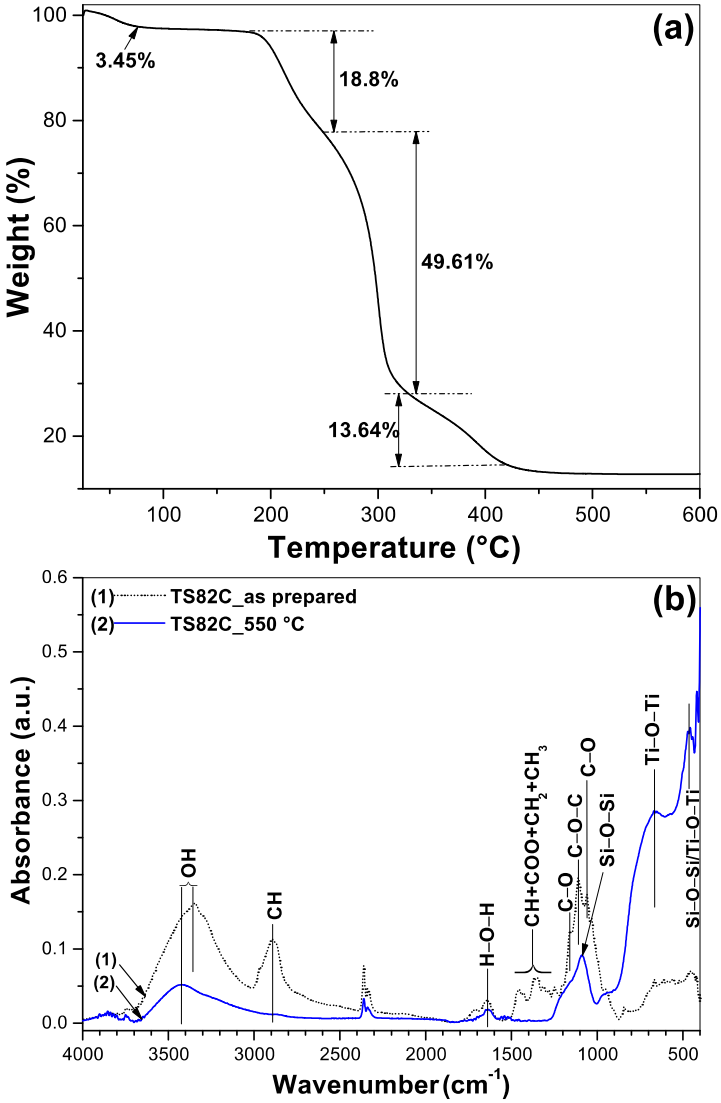

Figure 1. (**a**) Thermogravimetric analyses (TGA) of as prepared TS82C. (**b**) FTIR spectra of as prepared (curve 1) and 550 °C annealed (curve 2) TS82C.

The elimination of the organic templates from the composite sample after the calcination and determination of the structural information of TiO_2-SiO_2 was further supported by FTIR measurement. The FTIR spectra of the as prepared composite and after calcination at 550 °C are shown in Figure 1b. The as prepared sample (curve 1) shows a strong band around 3400 cm^{-1} due to the stretching vibration of hydroxyl groups coming from both the cellulose and TiO_2/SiO_2 matrices [30,37,39]. Other bands appeared at 2886, 1240–1490, 1158, and 1056 cm^{-1} could be assigned to CH, CH/COO/CH_2/CH_3, CO, and CO vibrations of the cellulose template [40,41]. It is noteworthy that the Si–O–Si asymmetric stretching band at 1086 cm^{-1} is superimposed by the strong C–O–C stretching vibration at 1110 cm^{-1} arising from the Pluronic template [42,43]. All the bands related to the organic species are indicated in Figure 1b. After annealing at 550 °C, all the bands related to the organic species disappeared, confirming their decomposition from the composite. At this stage, a new wide band centered at 668 cm^{-1} arose, which can be assigned to the characteristic stretching vibration of Ti–O–Ti coming from TiO_2 [39,44,45]. Another band at 465 cm^{-1} could be due to the Si–O–Si/Ti–O–Ti network of the composite. The strong appearance of the inorganic framework (Si/Ti–O–Si/Ti) at the lower wavenumber indicates the high degree of condensation in the inorganic network after the heat treatment [37].

3.2. Nanocrystalline Phase Composition and Mesoporosity

The crystalline nature and corresponding phase composition of the mixed nanocomposite was investigated using the powder XRD diffraction method and is shown in Figure 2a. All the diffraction peaks are assigned with their respective '*hkl*' parameters and were indexed as 25.32° (101), 36.98° (103), 37.84° (004), 38.56° (112), 48.05° (200), 53.98° (105), 55.12° (211), 62.79° (204), 68.84° (116), 70.31° (220), 75.15° (215), and 76.06° (301), which correspond to their pure anatase crystalline phases [45–47] (JCPDS No 84-1286). The average crystalline size calculated from XRD (Using Scherrer's formula, considering the strongest diffraction peak related to the 101 plane) was found to be 15.4 nm. The inset of Figure 2 shows the low-angle XRD pattern of the heat-treated sample where a strong reflection appears along with two other weaker reflections in the 2θ range of 0.5–2.5° with *d* spacings of 139.6, 98.07, and 68.96 Å. These peaks have *d* spacing ratios of ~$\sqrt{2}$:$\sqrt{4}$:$\sqrt{8}$, which can be indexed as (110), (200), and (220) reflections, respectively, corresponding to the cubic $Im\bar{3}m$ space group [43,48,49] with the lattice constant a = 197.4 Å. These data confirm the formation of SBA-16 type cubic mesoporous structures in our samples, which are expected when Pluronic F127 ($EO_{106}PO_{70}EO_{106}$) triblock copolymer is used as a structure-directing agent.

The result obtained in the XRD regarding the acquisition of a pure anatase crystalline phase is further supported by the Raman spectral measurement of the TS82C powder sample heat treated at 550 °C, shown in Figure 2b. The spectrum shows strong and well-resolved bands at 150, 201, 401, 516, 520 (superimposed with 516 cm^{-1} band), and 643 cm^{-1}, which can be attributed to the six characteristic Raman-active modes of anatase crystalline phase with the symmetries of E_g, E_g, B_{1g}, A_{1g}/B_{1g}, and E_g, respectively [46,48,50]. No other bands were observed, due to either the rutile or brookite crystalline phases [45].

The mesoporosity of the calcined TiO_2/SiO_2 nanocomposites was investigated by Brunauer–Emmett–Teller (BET) surface area measurements. The N_2 adsorption–desorption isotherms along with BJH pore-size distribution of calcined TS82 and TS82C are presented in Figure 3. The data for the commercial P25 TiO_2 powder is also shown for comparison. The full sets of data corresponding to the BET characterization of the mixed oxides with varying TiO_2/SiO_2 ratios are provided as Supporting Information (Figure S1, Table S1). All the plots show a type IV N_2 sorption isotherm, which is characteristic of the mesoporous structure [44,51–53]. Interestingly, the pure silica sample (Figure S1, sample TS01) displayed a more prominent H1 type hysteresis with a steep slope at a higher relative pressure due to capillary condensation in the mesopores, reflecting the formation of highly ordered mesopores and interparticle voids between the primary particles [52,54]. However, when increasing the amount of TiO_2 the hysteresis loop became wider, which is believed to be due to the presence of heterogeneous mesopores. This is evidenced by the multimodal

appearance and broadening of the BJH pore size distribution with the increasing amount of TiO_2 content (Figure S1, plot b). The pore size increased from 3.42 to 16.72 nm for the TS01 (SiO_2) and TS10 (TiO_2) samples, respectively. Consequently, the specific surface area also decreased from 553.31 (TS01) to 53.97 m^2g^{-1} (TS10) with the increasing wt% of TiO_2 (Table S1), which can be explained by the expansion of the pore size along with an increasing crystal size (Wide angle XRD analyses showed crystal size of 15.74 nm for TS73 and 17.55 nm for TS10) [52]. Now, if we compare BET analyses between TS82 and TS82C, the advantage of cellulose templating can be directly evaluated. TS82 displayed a specific surface area of 165.93 m^2g^{-1}, whereas for TS82C it was 186.82 m^2g^{-1}. Any significant changes in pore size distribution or pore volume were not noticed as reported in Table 1. So, the cellulose templating acted as the enhancer of the surface area of the composite, which in fact increased the photocatalytic efficiency (discussed later).

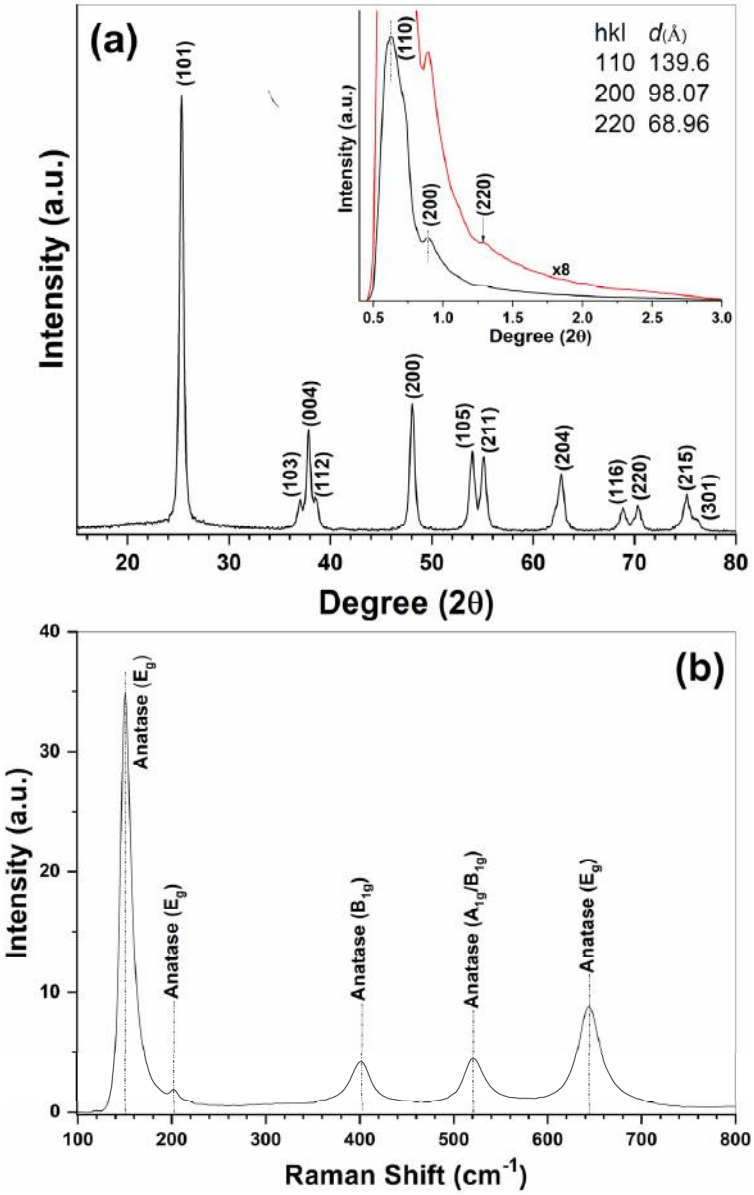

Figure 2. (**a**) Powder XRD pattern of the TS82C nanocomposite annealed at 550 °C. The inset shows low angle XRD pattern, where the hkl planes of the corresponding diffraction peaks along with the lattice spacings (*d*-values) are also shown. (**b**) Raman spectra of the TS82C powder calcined at 550 °C, showing different characteristic bands of the anatase crystalline phase.

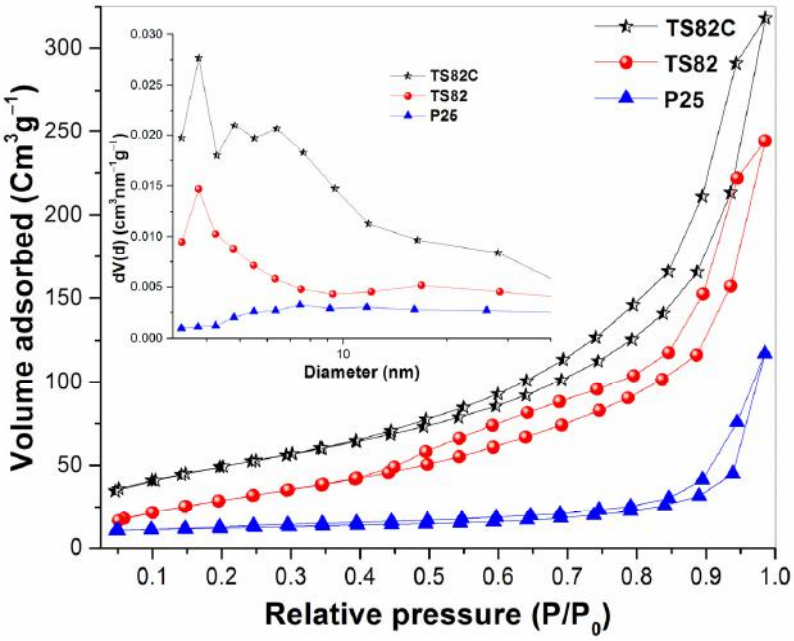

Figure 3. Nitrogen adsorption–desorption isotherm and BJH pore-size distribution plots (shown in inset) of TS82, TS82C nanocomposite calcined at 550 °C and P25 commercial (Evonik) TiO_2 powder.

Table 1. BET surface area parameters of the respective samples.

Sample	[a] S_{BET} (m^2g^{-1})	[b] D_{av} (nm)	[c] V (cm^3g^{-1})	[d] W_{xrd}		[e] D_{xrd}
				W_A	W_R	
TS82C	186.82	3.84	0.41	1.0	0	15.40
TS82	165.93	3.78	0.38	1.0	0	15.99
P25	38.25	7.61	0.17	0.84	0.16	22.16

[a] Specific surface area derived from the adsorption isotherm (P/P_0, 0.10−0.35). [b, c] Average pore diameter and pore volume calculated using BJH method from the desorption isotherm. [d] Anatase (W_A) and rutile (W_R) crystalline phase composition obtained from xrd analyses: $W_A = [1 + 1.26\ (I_{R110}/I_{A101})]^{-1}$; $W_R = [1 + 0.8\ (I_{A101}/I_{R110})]^{-1}$, I_{A101} and I_{R110} represents the integrated intensity of anatase (101 plane) and rutile (110 plane) diffraction peaks, respectively. [e] Average crystallite size estimated from the Scherrer's equation, $D_{xrd} = k\lambda/\beta Cos\theta$, where k is the shape factor (0.9), λ is the X-ray radiation wavelength (0.154 nm), β is the full width at half maxima of the corresponding Bragg angle (θ).

3.3. Microstructural Characterizations

The surface morphology of the TS82C composite was characterized by FESEM analyses, which is presented in Figure S2. The sample before calcination showed small sized nanoparticle formations grown along the cellulose microfibril's surface (Figure S2a,b), whereas after calcination the fibrous assembly disappeared leaving a porous structure where TiO_2 nanoparticles with an average size of 20–30 nm are distinctly visible (Figure S2c,d). To further analyze the microscopic particle structure and the arrangement of TiO_2/SiO_2, TEM measurements were performed on the calcined TS82C composite. Figure 4a shows the low magnification bright field image of TS82C, where two different contrasts are clearly distinguishable. Spherical TiO_2 nanoparticles with average size of about 20 nm could be identified from the dark contrast, whereas the lighter contrast corresponds to the amorphous silica support, forming a core-shell-like assembly, which is similar to the microscopic structure of TiO_2@SiO_2 composite reported by Yuan et al. [55]. So, it can be concluded that the nanocrystalline TiO_2 particles are well dispersed into the surrounding mesoporous silica matrix, which also prevents the aggregation of TiO_2 particles thus contributing to a higher surface area. Figure 4b,c show the high resolution images, where highly crystalline TiO_2 particles with an anatase phase are observed. This is also supported by the formation of high contrast diffraction rings presented in Figure 4d that closely matched the lattice

parameters obtained from the XRD result (Table 2). It is also noteworthy to observe some pores with diameter ranging from 3 to 4 nm (Figure 4b) that resemble the mesoporous structure of the TS82C nanocomposite supported by the BET measurements (Table 1), where an average pore diameter of 3.84 nm was observed.

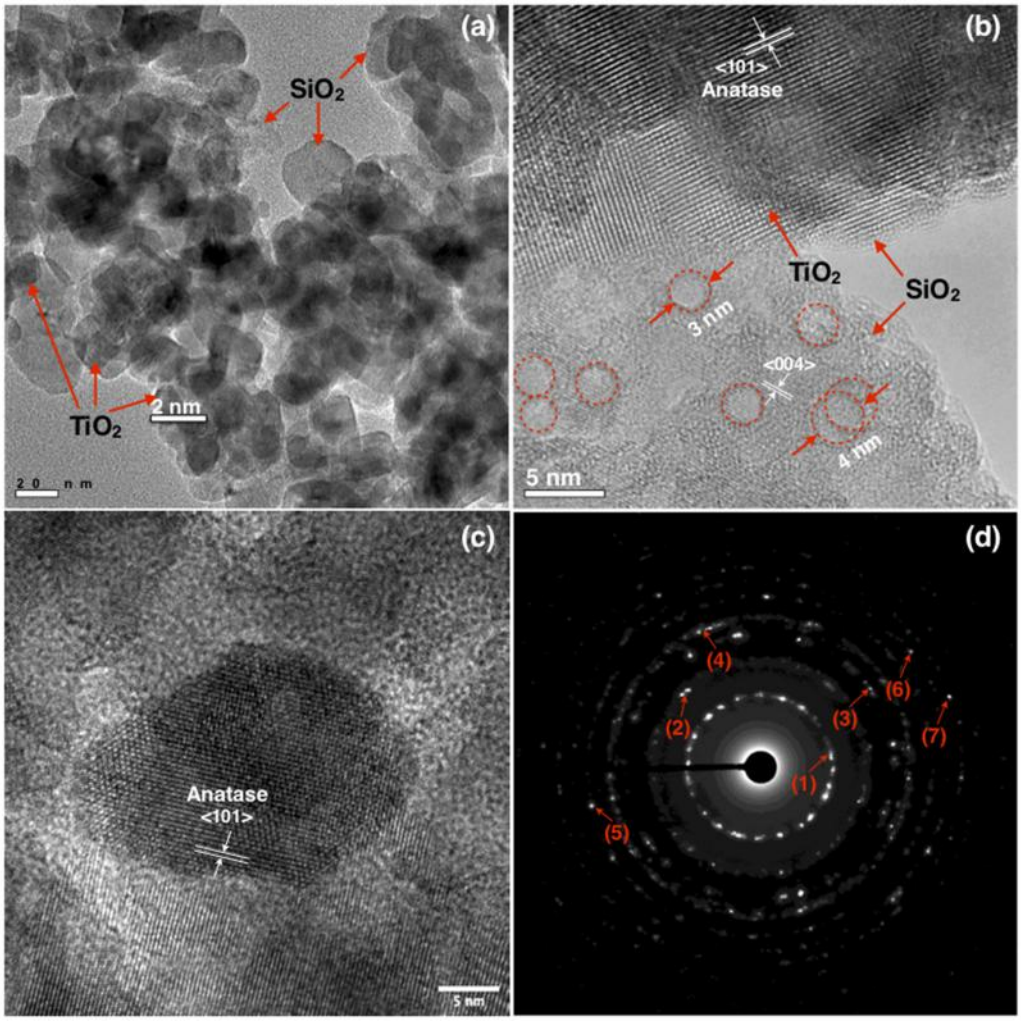

Figure 4. (**a**–**c**) TEM images showing morphology and crystallinity of TS82C composite calcined at 550 °C, (**a**) low magnification, (**b**,**c**) high resolution (HRTEM) images, and (**d**) selected area electron diffraction (SAED) pattern taken from image (**c**). The lattice spacing of the respective rings numbered in the SAED pattern is summarized in Table 2.

Table 2. Lattice parameters of the nanocrystalline TS82C calculated from SAED (Figure 4d) and XRD pattern (Figure 2a).

Diffraction Ring Number	[a] Lattice Spacing (d, Å)	Miller Indices (hkl)	[b] d_{XRD} (Å)
1	3.50	101	3.51
2	2.34	004	2.36
3	1.87	200	1.89
4	1.68	105	1.69
5	1.47	204	1.47
6	1.34	220	1.33
7	1.26	215	1.27

[a] Calculated using the camera equation, $d = \lambda L/R$, where λ is the wavelength of accelerated electron, L is the camera constant, and R is the radius of the corresponding diffraction ring. [b] Interplanar spacings obtained from 2θ values of the X-ray diffractogram (Figure 2).

3.4. Photocatalytic Activity

The photocatalytic activity of the TiO_2/SiO_2 composite samples was evaluated by the decomposition of three kinds of model pollutants, namely rhodamine B (RhB), Methylene blue (MB), and 4-Nitrophenol (4NP). Although RhB and MB dyes have been extensively studied as model pollutants that are commonly used in textile industries, Buriak et al. [56] suggested the inclusion of phenols as the model pollutant to compare the photodegradation efficiencies as the complete photodegradation of phenolic compounds is quite a difficult task. In fact, it is demonstrated that the reaction rate constant is much lower for 4NP (K value 0.025 min^{-1}) compared to RhB (K value 0.082 min^{-1}) and MB (K value 0.188 min^{-1}). The reaction parameters along with the half-life time are reported in Table 3. Degradation tests following the similar conditions were also performed with commercial P25 TiO_2 powder to compare the results. Figure 5a_1,b_1,c_1 show the degradation kinetics of RhB, MB, and 4NP, respectively. The evolution of the optical absorption spectra under light illumination of each pollutant performed with TS82C and P25 is shown in the (Supporting Information Figures S4–S6). It is clearly observed that in each case, the kinetic rate of dye degradation for TS82C is much higher than P25 TiO_2, which is well pronounced for its very high photocatalytic nature. It is also noteworthy that the degradation efficiency of TS82C is much higher in case of MB with a rate constant of 0.188 min^{-1}, and the lowest calculated half-life time of 3.68 min that might be due to the higher adsorption of MB on TS82C surfaces that triggers the photocatalytic activity by providing more active sites (Figure S5). As shown in Figures S4–S6, it is observed that the adsorption capacity of TS82C is much higher for RhB and MB dye molecules, whereas there is minimal adsorption for the 4NP dye molecules. This can be explained by the electrostatic interaction between the catalyst surface and the dye molecules. Having many hydroxyl groups present on the TS82C surface (evidenced from the FTIR spectra, Figure 1b) we can assume that in a near neutral environment, it would display surface negativity [57], thus attracting and trapping the cationic dye molecules into the porous network and consequently increasing the photodegradation efficiency. On the other hand, under identical experimental conditions, 4NP shows a tendency to exist in an anionic form [57], thus repelling the negatively charged TS82C surface showing poor adsorption and hence a lower photodegradation efficiency.

Table 3. Kinetic parameters of Rhodamine B, Methylene Blue and 4-Nitrophenol obtained from the photodegradation experiments performed with TS82C and P25 TiO_2.

Sample	Rhodamine B			Methylene Blue			4-Nitrophenol		
	[a] K	[b] $t_{1/2}$	[c] R^2	[a] K	[b] $t_{1/2}$	[c] R^2	[a] K	[b] $t_{1/2}$	[c] R^2
TS82C	0.082	8.45	0.98	0.188	3.68	0.97	0.025	27.72	0.88
P25	0.045	15.40	0.99	0.023	30.13	0.99	0.008	86.64	0.97

[a] Reaction rate constant, min^{-1}. [b] Half-life time of the respective organic dyes in minute calculated using the relation $t_{1/2} = \ln 2/K$, where K is the apparent reaction rate constant. [c] Coefficient of determination.

The reusability of the TS82C is reported in Figure 6, where three consecutive runs were performed using RhB, MB, and 4NP dyes. Although RhB and MB showed good consistency (4.8% and 12.2% less efficiency for 2nd and 3rd consecutive runs in case of RhB; 3.2% and 5.3% less efficiency for 2nd and 3rd runs in case of MB), a much lower efficiency was observed for 4NP with an increasing no. of runs (12% and 28% less efficiency for 2nd and 3rd run, respectively). A comparative study on the photocatalytic efficiency of various TiO_2/SiO_2 nanostructures is reported in Table S3. Although photocatalytic efficiency depends on various factors, such as light intensity, illumination, emitting wavelength, catalyst doses, dye concentration etc., Table S3 suggests that TS82C could perform well compared to those reported by the other researchers, particularly in solar photocatalysis. Despite having a lower reaction rate constant for 4NP compared to RhB and MB, TS82C shows a better performance than that reported for 4NP photodegradation [3,58]. Previous works on photocatalytic dye degradation suggest that the entrapment of the semiconductor

photocatalysts in amorphous silica matrix enhance the photoactivity [55]. Therefore, we can assume that the mesoporous nature and high surface area of TS82C play the key roles in photodegradation process. This is also evidenced from the much higher photodegradation efficiency of MB, where a higher adsorption was observed (Figure S5). Additionally, the stable anatase crystalline phase in TS82C provides a longer lifetime to the photogenerated electron-hole pairs and favors the adsorption site of the superoxide anions, which also contribute to the photocatalysis. The photogenerated charge carrier separation scenario within the TS82C nanocomposite was verified by the photoluminescence (PL) study and the PL spectra of TS82C and P25 TiO_2, as shown in Figure S7, where a relatively lower intensity of the PL spectra is observed for TS82C compared to P25 TiO_2. The lower PL signal suggests that the photogenerated electrons are trapped within the porous TS82C nanocomposite and transferred to the photocatalytic system, contributing to a higher photocatalytic efficiency.

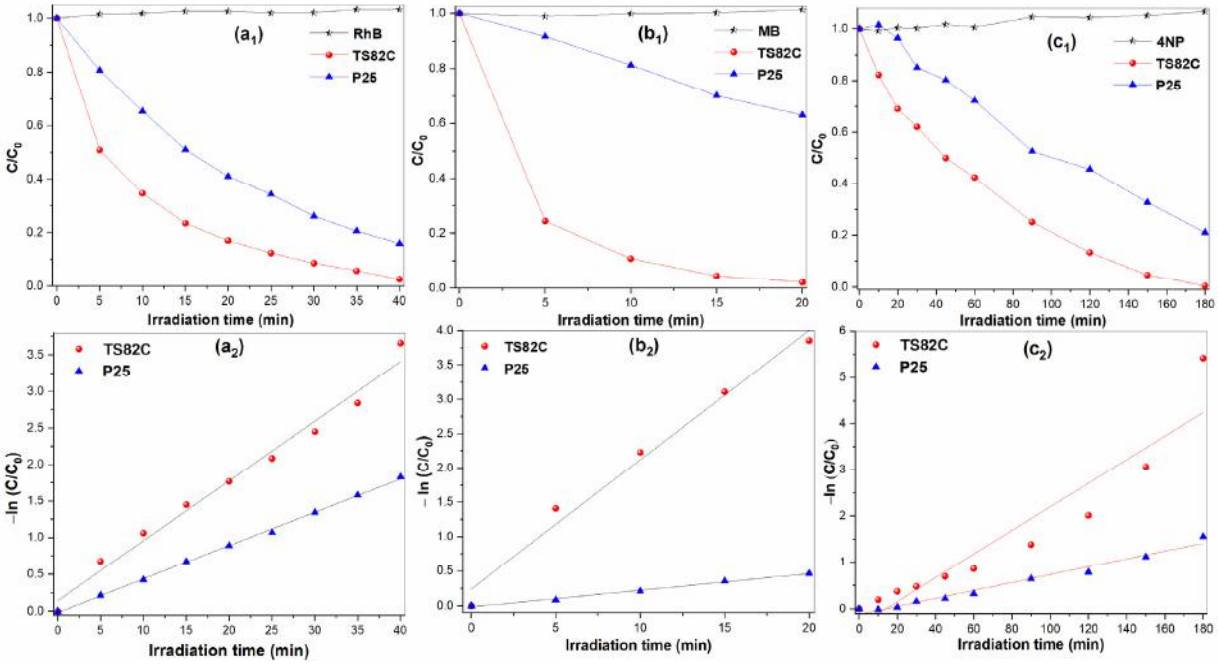

Figure 5. Photo-degradation kinetics of 15 µM aqueous solution of RhB ($\mathbf{a_1}$,$\mathbf{a_2}$), MB ($\mathbf{b_1}$,$\mathbf{b_2}$), and 4NP ($\mathbf{c_1}$,$\mathbf{c_2}$).

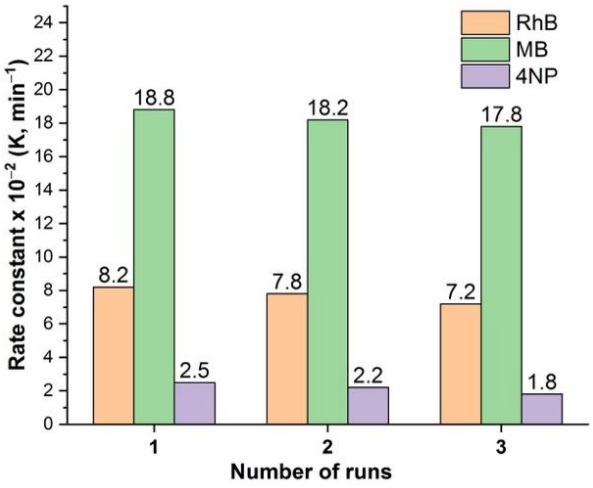

Figure 6. Reusability of TS82C photocatalyst by performing 3 consecutive runs with RhB, MB and 4NP dyes.

4. Conclusions

We have successfully synthesized cellulose and Pluronic F127 templated mesoporous TiO_2/SiO_2 nanocomposites with a higher specific surface area and higher thermal stability of the nanocrystalline anatase phase. An optimum level of silica incorporation (20% by weight) improved the anatase nanocrystalline phase stability, where cellulose/F127 soft-templating increased the mesoporosity while preserving the higher surface area. All the templating media were removed by thermal decomposition at 550 °C, as seen from the TGA/FTIR spectra; thus, a pure TiO_2/SiO_2 nanocomposite was obtained. The highly crystalline spherical TiO_2 particles were dispersed in a mesoporous silica structure as revealed by TEM analyses. The composite sample showed much higher photocatalytic efficiency than TiO_2/SiO_2 without the cellulose templating, and so did the standard reference catalyst P25 TiO_2. The photodegradation efficiency was tested against RhB, MB, and 4NP dyes under solar light irradiation. It could be said that the higher photocatalytic efficiency was achieved due to (i) the higher specific surface area, (ii) the formation of mesoporous structure, and (iii) the highly stable nanocrystalline anatase phase. The composite sample was not only effective against the commonly used dyes (RhB, MB), but also successfully decomposed nitro-aromatic compound (4NP), for which additional co-catalysts are required in the case of photodegradation. Since natural cellulose was used as a second templating, the catalyst powders could be prepared in large scale and eventually extended to synthesize other semiconductor photocatalysts and could find applications in water remediation technology and solar photocatalysis.

Supplementary Materials: The following supporting information can be downloaded at: https://www.mdpi.com/article/10.3390/catal12070770/s1, Table S1. Physicochemical properties of the TiO_2/SiO_2 composites; Figure S1. (a) N_2 adsorption–desorption isotherms and (b) pore size distribution plots of composite powders with different TiO_2/SiO_2 weight ratios; Figure S2. FESEM images of TS82C, (a, b) As prepared composite after drying, (c, d) after calcination at 550 °C; Figure S3. Photocatalytic degradation of RhB dye (15×10^{-6} M) with different TiO_2/SiO_2 photocatalysts; Table S2. Parameters of RhB dye degradation kinetics with different TiO_2/SiO_2 composites; Figure S4. Optical absorption spectra of RhB dye (15×10^{-6} M) with solar light exposure time performed with (a) TS82C and (b) P25 photocatalysts. The adsorption–desorption equilibrium was determined after stirring of 18 h at the dark; Figure S5. Optical absorption spectra of MB dye (15×10^{-6} M) with solar light exposure time performed with (a) TS82C and (b) P25 photocatalysts. The adsorption–desorption equilibrium was determined after stirring of 18 h in dark; Figure S6. Optical absorption spectra of 4NP compound (15×10^{-6} M) with solar light exposure time performed with (a) TS82C and (b) P25 photocatalysts. The adsorption–desorption equilibrium was determined after stirring of 18 h in dark; Figure S7. Photoluminescence (PL) spectra of TS82C nanocomposite (Red line) and P25 TiO_2 (Black line) measured on Horiba JOBIN YVON Fluoromax-P PL spectrophotometer using 365 nm as the excitation wavelength; Table S3. Comparative study of the photocatalytic activity with different TiO_2/SiO_2 photocatalysts [59–66].

Author Contributions: Conceptualization, S.P. and A.L.; methodology, S.P.; software, S.P. and A.T.; validation, S.P.; formal analysis, S.P.; investigation, S.P., A.T. and M.C.; data curation, S.P., A.T. and M.C.; writing—original draft preparation, S.P.; writing—review and editing, S.P. and A.L. All authors have read and agreed to the published version of the manuscript.

Funding: This research received no external funding.

Acknowledgments: The authors thankfully acknowledge Goutam De for providing the GIXRD facility, Fabio Marzo for performing the FESEM measurements, and Donato Cannoletta for recording the wide angle XRD spectra.

Conflicts of Interest: The authors declare no conflict of interest.

References

1. Hoffmann, M.R.; Martin, S.T.; Choi, W.; Bahnemann, D.W. Environmental Applications of Semiconductor Photocatalysis. *Chem. Rev.* **1995**, *95*, 69–96. [CrossRef]
2. Joseph, C.G.; Taufiq-Yap, Y.H.; Letshmanan, E.; Vijayan, V. Heterogeneous Photocatalytic Chlorination of Methylene Blue Using a Newly Synthesized TiO_2-SiO_2 Photocatalyst. *Catalysts* **2022**, *12*, 156. [CrossRef]
3. San, N.; Hatipoğlu, A.; Koçtürk, G.; Çınar, Z. Photocatalytic degradation of 4-nitrophenol in aqueous TiO_2 suspensions: Theoretical prediction of the intermediates. *J. Photochem. Photobiol. Chem.* **2002**, *146*, 189–197. [CrossRef]
4. Hashimoto, K.; Irie, H.; Fujishima, A. TiO_2 photocatalysis: A historical overview and future prospects. *Jpn. J. Appl. Phys.* **2005**, *44*, 8269. [CrossRef]
5. Chen, H.; Nanayakkara, C.E.; Grassian, V.H. Titanium Dioxide Photocatalysis in Atmospheric Chemistry. *Chem. Rev.* **2012**, *112*, 5919–5948. [CrossRef]
6. Dimitroula, H.; Daskalaki, V.M.; Frontistis, Z.; Kondarides, D.I.; Panagiotopoulou, P.; Xekoukoulotakis, N.P.; Mantzavinos, D. Solar photocatalysis for the abatement of emerging micro-contaminants in wastewater: Synthesis, characterization and testing of various TiO_2 samples. *Appl. Catal. B Environ.* **2012**, *117*, 283–291. [CrossRef]
7. He, Y.; Sutton, N.B.; Rijnaarts, H.H.H.; Langenhoff, A.A.M. Degradation of pharmaceuticals in wastewater using immobilized TiO_2 photocatalysis under simulated solar irradiation. *Appl. Catal. B Environ.* **2016**, *182*, 132–141. [CrossRef]
8. McCullagh, C.; Skillen, N.; Adams, M.; Robertson, P.K.J. Photocatalytic reactors for environmental remediation: A review. *J. Chem. Technol. Biotechnol.* **2011**, *86*, 1002–1017. [CrossRef]
9. Mills, A.; O'Rourke, C.; Moore, K. Powder semiconductor photocatalysis in aqueous solution: An overview of kinetics-based reaction mechanisms. *J. Photochem. Photobiol. Chem.* **2015**, *310*, 66–105. [CrossRef]
10. Maeda, K.; Domen, K. New Non-Oxide Photocatalysts Designed for Overall Water Splitting under Visible Light. *J. Phys. Chem. C* **2007**, *111*, 7851–7861. [CrossRef]
11. Fujishima, A.; Zhang, X.; Tryk, D.A. TiO_2 photocatalysis and related surface phenomena. *Surf. Sci. Rep.* **2008**, *63*, 515–582. [CrossRef]
12. Herrmann, J.-M. Photocatalysis fundamentals revisited to avoid several misconceptions. *Appl. Catal. B Environ.* **2010**, *99*, 461–468. [CrossRef]
13. Etacheri, V.; Seery, M.K.; Hinder, S.J.; Pillai, S.C. Oxygen Rich Titania: A Dopant Free, High Temperature Stable, and Visible-Light Active Anatase Photocatalyst. *Adv. Funct. Mater.* **2011**, *21*, 3744–3752. [CrossRef]
14. Joo, J.B.; Zhang, Q.; Lee, I.; Dahl, M.; Zaera, F.; Yin, Y. Mesoporous Anatase Titania Hollow Nanostructures though Silica-Protected Calcination. *Adv. Funct. Mater.* **2012**, *22*, 166–174. [CrossRef]
15. Yang, P.; Zhao, D.; Margolese, D.I.; Chmelka, B.F.; Stucky, G.D. Block Copolymer Templating Syntheses of Mesoporous Metal Oxides with Large Ordering Lengths and Semicrystalline Framework. *Chem. Mater.* **1999**, *11*, 2813–2826. [CrossRef]
16. Zhao, D.; Huo, Q.; Feng, J.; Chmelka, B.F.; Stucky, G.D. Nonionic Triblock and Star Diblock Copolymer and Oligomeric Surfactant Syntheses of Highly Ordered, Hydrothermally Stable, Mesoporous Silica Structures. *J. Am. Chem. Soc.* **1998**, *120*, 6024–6036. [CrossRef]
17. Araujo, P.Z.; Luca, V.; Bozzano, P.B.; Bianchi, H.L.; Soler-Illia, G.J.d.Á.A.; Blesa, M.A. Aerosol-Assisted Production of Mesoporous Titania Microspheres with Enhanced Photocatalytic Activity: The Basis of an Improved Process. *ACS Appl. Mater. Interfaces* **2010**, *2*, 1663–1673. [CrossRef]
18. Ismail, A.A.; Bahnemann, D.W. Mesoporous titania photocatalysts: Preparation, characterization and reaction mechanisms. *J. Mater. Chem.* **2011**, *21*, 11686–11707. [CrossRef]
19. Choi, S.Y.; Mamak, M.; Coombs, N.; Chopra, N.; Ozin, G.A. Thermally Stable Two-Dimensional Hexagonal Mesoporous Nanocrystalline Anatase, Meso-nc-TiO_2: Bulk and Crack-Free Thin Film Morphologies. *Adv. Funct. Mater.* **2004**, *14*, 335–344. [CrossRef]
20. Mahoney, L.; Koodali, R.T. Versatility of Evaporation-Induced Self-Assembly (EISA) Method for Preparation of Mesoporous TiO_2 for Energy and Environmental Applications. *Materials* **2014**, *7*, 2697–2746. [CrossRef]
21. Chen, L.; Yao, B.; Cao, Y.; Fan, K. Synthesis of Well-Ordered Mesoporous Titania with Tunable Phase Content and High Photoactivity. *J. Phys. Chem. C* **2007**, *111*, 11849–11853. [CrossRef]
22. Wang, W.; Nguyen, D.; Long, H.; Liu, G.; Li, S.; Yue, X.; Ru, H. High temperature and water-based evaporation-induced self-assembly approach for facile and rapid synthesis of nanocrystalline mesoporous TiO_2. *J. Mater. Chem. A* **2014**, *2*, 15912–15920. [CrossRef]
23. Hirano, M.; Ota, K.; Iwata, H. Direct Formation of Anatase (TiO_2)/Silica (SiO_2) Composite Nanoparticles with High Phase Stability of 1300 °C from Acidic Solution by Hydrolysis under Hydrothermal Condition. *Chem. Mater.* **2004**, *16*, 3725–3732. [CrossRef]
24. Dong, W.; Sun, Y.; Lee, C.W.; Hua, W.; Lu, X.; Shi, Y.; Zhang, S.; Chen, J.; Zhao, D. Controllable and Repeatable Synthesis of Thermally Stable Anatase Nanocrystal−Silica Composites with Highly Ordered Hexagonal Mesostructures. *J. Am. Chem. Soc.* **2007**, *129*, 13894–13904. [CrossRef]
25. Chen, S.-Y.; Tang, C.-Y.; Lee, J.-F.; Jang, L.-Y.; Tatsumi, T.; Cheng, S. Effect of calcination on the structure and catalytic activities of titanium incorporated SBA-15. *J. Mater. Chem.* **2011**, *21*, 2255–2265. [CrossRef]

26. Pierpaoli, M.; Zheng, X.; Bondarenko, V.; Fava, G.; Ruello, M.L. Paving the Way for A Sustainable and Efficient SiO_2/TiO_2 Photocatalytic Composite. *Environments* **2019**, *6*, 87. [CrossRef]
27. Eddy, D.R.; Ishmah, S.N.; Permana, M.D.; Firdaus, M.L. Synthesis of Titanium Dioxide/Silicon Dioxide from Beach Sand as Photocatalyst for Cr and Pb Remediation. *Catalysts* **2020**, *10*, 1248. [CrossRef]
28. Temerov, F.; Haapanen, J.; Mäkelä, J.M.; Saarinen, J.J. Photocatalytic Activity of Multicompound TiO_2/SiO_2 Nanoparticles. *Inorganics* **2021**, *9*, 21. [CrossRef]
29. Mohamed, M.A.; Salleh, W.W.; Jaafar, J.; Ismail, A.F.; Mutalib, M.A.; Sani, N.; Asri, S.M.; Ong, C. Physicochemical characteristic of regenerated cellulose/N-doped TiO_2 nanocomposite membrane fabricated from recycled newspaper with photocatalytic activity under UV and visible light irradiation. *Chem. Eng. J.* **2016**, *284*, 202–215. [CrossRef]
30. Zeng, J.; Liu, S.; Cai, J.; Zhang, L. TiO_2 Immobilized in Cellulose Matrix for Photocatalytic Degradation of Phenol under Weak UV Light Irradiation. *J. Phys. Chem. C* **2010**, *114*, 7806–7811. [CrossRef]
31. Liu, X.; Gu, Y.; Huang, J. Hierarchical, Titania-Coated, Carbon Nanofibrous Material Derived from a Natural Cellulosic Substance. *Chem.—Eur. J.* **2010**, *16*, 7730–7740. [CrossRef] [PubMed]
32. Postnova, I.; Kozlova, E.; Cherepanova, S.; Tsybulya, S.; Rempel, A.; Shchipunov, Y. Titania synthesized through regulated mineralization of cellulose and its photocatalytic activity. *RSC Adv.* **2015**, *5*, 8544–8551. [CrossRef]
33. Plumejeau, S.; Rivallin, M.; Brosillon, S.; Ayral, A.; Boury, B. M-Doped TiO_2 and TiO_2–MxOy Mixed Oxides (M = V, Bi, W) by Reactive Mineralization of Cellulose—Evaluation of Their Photocatalytic Activity. *Eur. J. Inorg. Chem.* **2016**, *2016*, 1200–1205. [CrossRef]
34. Liciulli, A.; Nisi, R.; Pal, S.; Laera, A.M.; Creti, P.; Chiechi, A. Photo-oxidation of ethylene over mesoporous TiO_2/SiO_2 catalysts. *Adv. Hortic. Sci.* **2016**, *30*, 75–80. [CrossRef]
35. de Chiara, M.; Pal, S.; Licciulli, A.; Amodio, M.; Colelli, G. Photocatalytic degradation of ethylene on mesoporous TiO_2/SiO_2 nanocomposites: Effects on the ripening of mature green tomatoes. *Biosyst. Eng.* **2015**, *132*, 61–70. [CrossRef]
36. Hongo, T.; Yamazaki, A. Thermal influence on the structure and photocatalytic activity of mesoporous titania consisting of TiO_2(B). *Microporous Mesoporous Mater.* **2011**, *142*, 316–321. [CrossRef]
37. Crepaldi, E.L.; Soler-Illia, G.J.D.A.A.; Bouchara, A.; Grosso, D.; Durand, D.; Sanchez, C. Controlled Formation of Highly Ordered Cubic and Hexagonal Mesoporous Nanocrystalline Yttria–Zirconia and Ceria–Zirconia Thin Films Exhibiting High Thermal Stability. *Angew. Chem. Int. Ed.* **2003**, *42*, 347–351. [CrossRef]
38. Luo, Y.; Xu, J.; Huang, J. Hierarchical nanofibrous anatase-titania–cellulose composite and its photocatalytic property. *CrystEngComm* **2014**, *16*, 464–471. [CrossRef]
39. Padmanabhan, S.K.; Pal, S.; Haq, E.U.; Licciulli, A. Nanocrystalline TiO_2–diatomite composite catalysts: Effect of crystallization on the photocatalytic degradation of rhodamine B. *Appl. Catal. Gen.* **2014**, *485*, 157–162. [CrossRef]
40. Cunha, A.G.; Freire, C.S.R.; Silvestre, A.J.D.; Neto, C.P.; Gandini, A.; Orblin, E.; Fardim, P. Highly Hydrophobic Biopolymers Prepared by the Surface Pentafluorobenzoylation of Cellulose Substrates. *Biomacromolecules* **2007**, *8*, 1347–1352. [CrossRef]
41. Ciolacu, D.; Ciolacu, F.; Popa, V.I. Amorphous cellulose—Structure and characterization. *Cellul. Chem. Technol.* **2011**, *45*, 13.
42. Carboni, D.; Marongiu, D.; Rassu, P.; Pinna, A.; Amenitsch, H.; Casula, M.; Marcelli, A.; Cibin, G.; Falcaro, P.; Malfatti, L.; et al. Enhanced Photocatalytic Activity in Low-Temperature Processed Titania Mesoporous Films. *J. Phys. Chem. C* **2014**, *118*, 12000–12009. [CrossRef]
43. Saha, J.; De, G. Highly ordered cubic mesoporous electrospun SiO_2 nanofibers. *Chem. Commun.* **2013**, *49*, 6322–6324. [CrossRef]
44. Chattopadhyay, S.; Saha, J.; De, G. Electrospun anatase TiO_2 nanofibers with ordered mesoporosity. *J. Mater. Chem. A* **2014**, *2*, 19029–19035. [CrossRef]
45. Pal, S.; Laera, A.M.; Licciulli, A.; Catalano, M.; Taurino, A. Biphase TiO_2 Microspheres with Enhanced Photocatalytic Activity. *Ind. Eng. Chem. Res.* **2014**, *53*, 7931–7938. [CrossRef]
46. Parra, R.; Góes, M.S.; Castro, M.S.; Longo, E.; Bueno, P.R.; Varela, J.A. Reaction Pathway to the Synthesis of Anatase via the Chemical Modification of Titanium Isopropoxide with Acetic Acid. *Chem. Mater.* **2008**, *20*, 143–150. [CrossRef]
47. De Ceglie, C.; Pal, S.; Murgolo, S.; Licciulli, A.; Mascolo, G. Investigation of Photocatalysis by Mesoporous Titanium Dioxide Supported on Glass Fibers as an Integrated Technology for Water Remediation. *Catalysts* **2022**, *12*, 41. [CrossRef]
48. Yang, P.; Zhao, D.; Margolese, D.I.; Chmelka, B.F.; Stucky, G.D. Generalized syntheses of large-pore mesoporous metal oxides with semicrystalline frameworks. *Nature* **1998**, *396*, 152–155. [CrossRef]
49. Zhao, D.; Yang, P.; Melosh, N.; Feng, J.; Chmelka, B.F.; Stucky, G.D. Continuous Mesoporous Silica Films with Highly Ordered Large Pore Structures. *Adv. Mater.* **1998**, *10*, 1380–1385. [CrossRef]
50. Zhang, J.; Li, M.; Feng, Z.; Chen, J.; Li, C. UV Raman Spectroscopic Study on TiO_2. I. Phase Transformation at the Surface and in the Bulk. *J. Phys. Chem. B* **2006**, *110*, 927–935. [CrossRef]
51. Sing, K.S.W. Reporting Physisorption Data for Gas/Solid Systems with Special Reference to the Determination of Surface Area and Porosity. *Pure Appl. Chem.* **1985**, *57*, 603–619. [CrossRef]
52. Chen, D.; Huang, F.; Cheng, Y.-B.; Caruso, R.A. Mesoporous Anatase TiO_2 Beads with High Surface Areas and Controllable Pore Sizes: A Superior Candidate for High-Performance Dye-Sensitized Solar Cells. *Adv. Mater.* **2009**, *21*, 2206–2210. [CrossRef]
53. Luo, Z.; Poyraz, A.S.; Kuo, C.-H.; Miao, R.; Meng, Y.; Chen, S.-Y.; Jiang, T.; Wenos, C.; Suib, S.L. Crystalline Mixed Phase (Anatase/Rutile) Mesoporous Titanium Dioxides for Visible Light Photocatalytic Activity. *Chem. Mater.* **2015**, *27*, 6–17. [CrossRef]

54. Ko, Y.G.; Lee, H.J.; Kim, J.Y.; Choi, U.S. Hierarchically Porous Aminosilica Monolith as a CO_2 Adsorbent. *ACS Appl. Mater. Interfaces* **2014**, *6*, 12988–12996. [CrossRef] [PubMed]
55. Yuan, L.; Han, C.; Pagliaro, M.; Xu, Y.-J. Origin of Enhancing the Photocatalytic Performance of TiO_2 for Artificial Photoreduction of CO_2 through a SiO_2 Coating Strategy. *J. Phys. Chem. C* **2016**, *120*, 265–273. [CrossRef]
56. Buriak, J.M.; Kamat, P.V.; Schanze, K.S. Best Practices for Reporting on Heterogeneous Photocatalysis. *ACS Appl. Mater. Interfaces* **2014**, *6*, 11815–11816. [CrossRef]
57. Deng, F.; Liu, Y.; Luo, X.; Wu, S.; Luo, S.; Au, C.; Qi, R. Sol-hydrothermal synthesis of inorganic-framework molecularly imprinted TiO_2/SiO_2 nanocomposite and its preferential photocatalytic degradation towards target contaminant. *J. Hazard. Mater.* **2014**, *278*, 108–115. [CrossRef]
58. Rezaei-Vahidian, H.; Zarei, A.R.; Soleymani, A.R. Degradation of nitro-aromatic explosives using recyclable magnetic photocatalyst: Catalyst synthesis and process optimization. *J. Hazard. Mater.* **2017**, *325*, 310–318. [CrossRef]
59. Kim, Y.N.; Shao, G.N.; Jeon, S.J.; Imran, S.M.; Sarawade, P.B.; Kim, H.T. Gel Synthesis of Sodium Silicate and Titanium Oxychloride Based TiO_2–SiO_2 Aerogels and Their Photocatalytic Property under UV Irradiation. *Chem. Eng. J.* **2013**, *231*, 502–511. [CrossRef]
60. Mahanta, U.; Khandelwal, M.; Deshpande, A.S. TiO_2@SiO_2 Nanoparticles for Methylene Blue Removal and Photocatalytic Degradation under Natural Sunlight and Low-Power UV Light. *Appl. Surf. Sci.* **2022**, *576*, 151745. [CrossRef]
61. Bao, Y.; Guo, R.; Gao, M.; Kang, Q.; Ma, J. Morphology Control of 3D Hierarchical Urchin-like Hollow SiO_2@TiO_2 Spheres for Photocatalytic Degradation: Influence of Calcination Temperature. *J. Alloys Compd.* **2021**, *853*, 157202. [CrossRef]
62. Ferreira-Neto, E.P.; Ullah, S.; Simões, M.B.; Perissinotto, A.P.; de Vicente, F.S.; Noeske, P.-L.M.; Ribeiro, S.J.L.; Rodrigues-Filho, U.P. Solvent-Controlled Deposition of Titania on Silica Spheres for the Preparation of SiO_2@TiO_2 Core@shell Nanoparticles with Enhanced Photocatalytic Activity. *Colloids Surf. A Physicochem. Eng. Asp.* **2019**, *570*, 293–305. [CrossRef]
63. Guo, N.; Liang, Y.; Lan, S.; Liu, L.; Ji, G.; Gan, S.; Zou, H.; Xu, X. Uniform TiO_2–SiO_2 Hollow Nanospheres: Synthesis, Characterization and Enhanced Adsorption–Photodegradation of Azo Dyes and Phenol. *Appl. Surf. Sci.* **2014**, *305*, 562–574. [CrossRef]
64. Palhares, H.G.; Nunes, E.H.M.; Houmard, M. Heat Treatment as a Key Factor for Enhancing the Photodegradation Performance of Hydrothermally-Treated Sol–Gel TiO_2–SiO_2 Nanocomposites. *J. Sol-Gel Sci. Technol.* **2021**, *99*, 188–197. [CrossRef]
65. Bellardita, M.; Addamo, M.; Di Paola, A.; Marcì, G.; Palmisano, L.; Cassar, L.; Borsa, M. Photocatalytic Activity of TiO_2/SiO_2 Systems. *J. Hazard. Mater.* **2010**, *174*, 707–713. [CrossRef]
66. Liao, S.; Lin, L.; Huang, J.; Jing, X.; Chen, S.; Li, Q. Microorganism-Templated Nanoarchitectonics of Hollow TiO_2-SiO_2 Microspheres with Enhanced Photocatalytic Activity for Degradation of Methyl Orange. *Nanomaterials* **2022**, *12*, 1606. [CrossRef]